Thermal dewetting with a chemically heterogeneous nano-template for self-assembled $L1_0$ FePt nanoparticle arrays†

Liang-Wei Wang‡ [a], **Chung-Fu Cheng‡** [a], **Jung-Wei Liao** [a], **Chiu-Yen Wang** [b], **Ding-Shuo Wang** [a], **Kuo-Feng Huang** [a], **Tzu-Ying Lin** [a], **Rong-Ming Ho** [c], **Lih-Juann Chen** [a] **and Chih-Huang Lai** *[a]

[a]*Department of Materials Science and Engineering, National Tsing Hua University, Hsinchu 30013, Taiwan. E-mail: chlai@mx.nthu.edu.tw*

[b]*Department of Materials Science and Engineering, National Taiwan University of Science and Technology, Taipei 10607, Taiwan*

[c]*Department of Chemical Engineering, National Tsing Hua University, Hsinchu 30013, Taiwan*

Received 25th November 2015 , Accepted 24th January 2016

First published on 26th January 2016

A design for the fabrication of metallic nanoparticles is presented by thermal dewetting with a chemically heterogeneous nano-template. For the template, we fabricate a nanostructured polystyrene-*b*-polydimethylsiloxane (PS-*b*-PDMS) film on a Si|SiO_2 substrate, followed by a thermal annealing and reactive ion etching (RIE) process. This gives a template composed of an ordered hexagonal array of SiOC hemispheres emerging in the polystyrene matrix. After the deposition of a FePt film on this template, we utilize the rapid thermal annealing (RTA) process, which provides in-plane stress, to achieve thermal dewetting and structural ordering of FePt simultaneously. Since the template is composed of different composition surfaces with periodically varied morphologies, it offers more tuning knobs to manipulate

the nanostructures. We show that both the decrease in the area of the PS matrix and the increase in the strain energy relaxation transfer the dewetted pattern from the randomly distributed nanoparticles into a hexagonal periodic array of $L1_0$ FePt nanoparticles. Transmission electron microscopy with the *in situ* heating stage reveals the evolution of the dewetting process, and confirms that the positions of nanoparticles are aligned with those of the SiOC hemispheres. The nanoparticles formed by this template-dewetting show an average diameter and center-to-center distance of 19.30 ± 2.09 nm and 39.85 ± 4.80 nm, respectively. The hexagonal array of FePt nanoparticles reveals a large coercivity of 1.5 T, much larger than the nanoparticles fabricated by top-down approaches. This approach offers an efficient pathway toward self-assembled nanostructures in a wide range of material systems.

1. Introduction

Metallic nanoparticles and nanostructures have attracted considerable interest for potential applications in bit-patterned magnetic recording media,[1–3] plasmonic waveguides,[4–6] and catalysts for the growth of nanowires and nanotubes.[7–9] For fabrications of the nano-patterns, the typical methods can be divided into two categories: top-down[10–12] and bottom-up approaches.[13] Among the top-down methods, electron-beam lithography has been demonstrated to fabricate nano-patterns with controllable features.[10,12] Yet the low throughput of this lithography method significantly narrows its applicability.[12] In addition, as the feature sizes of patterns are continuously decreased, the processing damage associated with the ion milling during etching may significantly alter the nano-pattern properties.[14,15] On the other hand, a promising route of the bottom-up methods to realize mono-disperse nanoparticles is chemical synthesis.[13,16] In this approach one of challenges is the removal of the surfactant from particle surfaces.[13] The remaining surfactant makes the fabricated particles difficult for surface-sensitive applications, *e.g.*, catalysts for growing nanowires or fuel cells.

Alternatively, for fabrication of surfactant-free metal nanoparticles, solid-state dewetting of thin films has long been considered as an efficient pathway.[17–19] Dewetting is a process of a thin film uncovering from a substrate

surface at elevated temperatures and is driven by minimizing the total surface energy in the film–substrate system. The morphology gradually changes from a continuous film to individual nanoparticles with increasing temperature.[20] Although this approach has been demonstrated to obtain nanoparticle dewetting on a flat substrate with average diameters well below 100 nm, the grain boundaries and grain sizes in the as-deposited films determine the initially nucleated position of dewetting, resulting in a broad distribution of particle sizes and random dispersion.[19] To achieve ordered particle arrays by dewetting, templated dewetting has been proposed.[19,21–25] In this controlled manner, the substrate topography is first patterned into ordered features with periodical variations in the surface curvature, followed by film deposition. Because the surface chemical potential is proportional to the curvature of the substrate surface,[26] relative to a flat substrate surface, the excess chemical potential is positive at convex regions but is negative at concave areas. As the temperature increases, the differential chemical potential results in void nucleation at the edges of holes and the subsequent assembly of particles either into or around holes (concave areas). By utilizing this approach, Giermann and Thompson have fabricated ordered Au nanoparticle arrays on photo-lithographically patterned Si substrates with 175 nm-period inverse pyramidal pits.[21] On the similarly patterned Si substrates, Oh *et al.* have demonstrated both Co[22] and the CoPt nanoparticle arrays.[23] Lei *et al.* have utilized Si templates patterned by polystyrene spheres to obtain Au, Ag, and AuAg particle arrays.[24] The diameter of the fabricated particles is around a few hundred nanometers.[21–24] For template dewetting with the photo-lithographically patterned templates, the feature size of nanostructures is restricted by the diffraction limit. To drive the topographic period below 50 nm, non-lithographically patterned templates are necessary. Hart *et al.* have recently used anodized alumina (AAO) with 49

nm-period holes as the template to fabricate Fe nanoparticle arrays, which possess local hexagonal ordering.[25]

In addition, dewetting behaviors of films grown on a non-solid substrate template of poly(methyl methacrylate) (PMMA) have also been investigated.[27,28] The dewetting process also occurs in the non-solid PMMA template during the film dewetting process, and this substrate dewetting is capable of manipulating the resulting film patterns on top of the substrate. By utilizing this technique, the different Au nanopatterns dewetted on the PMMA substrates have been demonstrated.[27,28]

In addition to substrate morphologies, the introduction of strain in films during dewetting has been reported to modify the surface chemical potential.[29] The variations of strain energy can alter the local minima of chemical potential to be in the convex regions of substrates, leading to the formation of dewetted particles in these areas. This would be quite desirable for the applications of patterned magnetic recording media and catalysts, for which nanoparticles located at the top of nano-templates instead of in holes are preferred. Using this strain-mediated chemical potential, Lagally *et al.* have demonstrated dewetted Ge dots on the ridges (the convex regions), instead of in the valley (the concave regions), of patterned Si (001) substrates.[29] In this case, the Ge layer is hetero-epitaxially grown on the Si substrates. Therefore, the lattice mismatch between Ge and Si gives rise to strain energy in the Ge layers.

Here, we present a novel approach to obtain a periodic $L1_0$ FePt nanoparticle array by using thermal dewetting with a chemically heterogeneous template. This nano-template, fabricated from the polystyrene-*b*-poly(dimethylsiloxane) (PS-*b*-PDMS) block copolymer (BCP), is composed of hexagonal-packed SiOC hemisphere arrays emerging in the polystyrene (PS) matrix. Because SiOC hemispheres can be self-assembled

and their sizes can be controlled down to 25 nm, they reveal great potential for template-dewetting to achieve a regular nanoparticle array with the feature size below 25 nm. Different from the reported template-dewetting with a chemically homogeneous interface between the film and substrate, that is, the template surface consisting of the same composition but with various morphologies, our chemically heterogeneous nano-template, SiOC + PS matrix, enables us to spatially vary the interfacial diffusion rate and the strain energy in different compositional regions. Consequently, our FePt nanoparticles are located on apexes of nano-templates with a unique volcano shape, different from most of the reported studies, in which the nanoparticles are located in the holes or flat regions of the templates due to the curvature-driven chemical potential difference.[21–24,26] The distinct driving force for FePt dewetting on the proposed nano-template is the strain energy difference, originating from the varied degree of FePt structural ordering on different surfaces (SiOC or PS).

We choose a FePt alloy as the target material because it is regarded as a promising candidate for broad applications, *e.g.*, the next-generation recording media[30] and catalysts for the growth of carbon nanotubes.[31] Furthermore, the nanocrystals of Pt alloys (including FePt) in general can serve as catalysts for cathodic oxygen reduction[32,33] and improve the durability of electrodes in fuel cells.[34,35] Additionally, the FePt film is under a phase transformation from a disordered A1 phase to an ordered $L1_0$ phase at an annealing temperature higher than 500 °C.[36] Self-assembled FePt $L1_0$ nanoparticle arrays are difficult to achieve by using chemically synthesized nanoparticles due to the particle aggregation after annealing at high temperature to form the $L1_0$ phase.[37] Therefore, the template-dewetting process may not only form self-assembled nanoparticles but simultaneously complete the phase transformation.

2. Experimental

2.1 Preparation of well-ordered SiOC dot array

The topographic templates consisted of hexagonal-packed SiOC sphere arrays with a diameter of 25 nm and center-to-center spacing of 40 nm on thermally oxidized Si substrates. The disordered PS-*b*-PDMS films were spin-coated on thermally oxidized Si substrates from the 2 wt% solution of the BCP in toluene. The molecular weights of PS and PDMS were 33.2 kg mol^{-1} and 14.0 kg mol^{-1}, respectively. The volume fraction of the PDMS block was 0.32. After spin-coating, the PS-*b*-PDMS films were annealed at 200 °C for 1 hour to change the PDMS spheres into ordered hexagonal packing. The samples were subsequently treated with CF_4 and O_2 plasma in sequence to respectively remove the thin PDMS surface layer and to selectively etch the PS matrix while oxidizing the PDMS spheres. The CF_4 and O_2 plasma were generated by a RF power source in a reactive ion etching (RIE) system, and the processing parameters were 50 W, 20 s at a pressure of 75 mTorr for CF_4 treatment and 100 W, 10–30 s at 60 mTorr for O_2 etching, respectively.

2.2 Deposition of FePt film and characterization

$Fe_{52}Pt_{48}$ films with the nominal thickness of 2 or 5 nm were co-sputtered from elemental targets at room temperature. The composition of $Fe_{52}Pt_{48}$ was determined by inductively coupled plasma-mass spectrometry. After film deposition, the samples were annealed at 800 °C for 10 seconds using the rapid-thermal annealing (RTA) system. Magnetic properties were determined by using a superconducting quantum interference device with a maximum field of 70 kOe. Surface topographies of samples were obtained by using an atomic force microscope (AFM). A Seiko SPA-400 AFM with a Seiko SPI-3800N probe station was utilized at room temperature to obtain tapping-mode AFM images. A rectangular silicon tip was used in the dynamic force mode with a spring force of 5 N m^{-1}, tip size about 3 nm and a scan rate of 1 Hz. Sample microstructures were investigated using a transmission electron microscope (TEM). For the TEM (JEOL 2010) observation with *in situ* heating, the Gatan 652 double tilt heating holder was utilized. This holder was connected to a power supply, which provided an electric current at a current density of 2–3 $\times 10^6$ A cm^{-2} to heat the specimen, and a temperature controller for monitoring sample temperature. Using this holder, the sample temperature during TEM observation was varied from room temperature to 1000 °C with a heating rate of 50 °C min^{-1}, while the TEM images were video recorded in real time.

3. Results and discussion

3.1 Thermal dewetting of FePt on chemically heterogeneous surface

Fig. 1 illustrates the fabrication process of FePt nanoparticles dewetted on the topographic template, composed of a SiOC hemisphere array in a PS matrix coated on a Si|SiO_2 (200 nm) substrate. The PS-*b*-PDMS BCP (M_w = 47

kg mol^{-1}) with a PDMS volume fraction (f_{PDMS}) of 32% was first dissolved in a common solvent (*i.e.* toluene) with 2 wt%, followed by spin-coating onto the substrates to form a disordered PS-*b*-PDMS film [Fig. 1(a)]. With a slight preference of solvent to PS, the PDMS formed spheres embedded in the PS matrix. The samples were then annealed in a vacuum oven at 200 °C for 1 h to change the lateral order of PDMS spheres into a hexagonal array. In addition, due to the relatively small surface energy of PDMS, a PDMS wetting layer formed on top of the BCP film [Fig. 1(b)]. After annealing, we performed the reactive ion etching (RIE) process in which the CF_4 plasma was first used to remove the PDMS wetting layer, followed by utilizing the O_2 plasma to selectively reduce the thickness of the PS matrix while oxidizing the PDMS into the SiOC hemisphere array. Consequently, a nano-template composed of a chemically heterogeneous surface with periodically varied morphology is achieved for thermal dewetting [Fig. 1(c)]. We subsequently sputtered the FePt film on this topographic template at ambient temperature [Fig. 1(d)] and then performed a rapid-thermal annealing process for thermal dewetting [Fig. 1(e)].

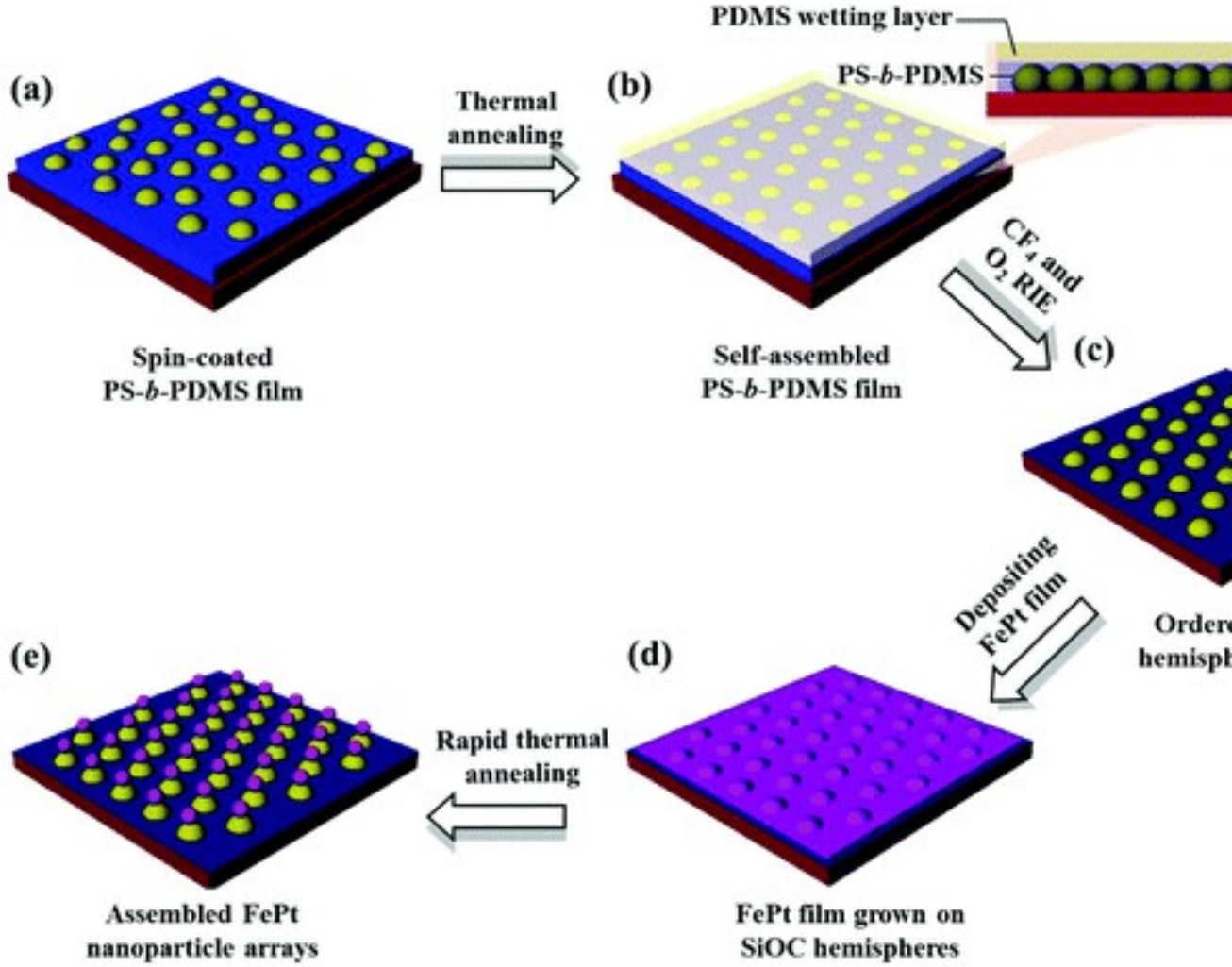

Fig. 1 (Color on-line) Schematic diagrams of the fabrication process of $L1_0$ FePt nanoparticle arrays self-assemb

template.

BCP films have been previously demonstrated to possess broad feasibility for nanopatterns with feature sizes well below 50 nm.[38–40] However, the template fabricated with a regular phase-separation process for BCP (for example, polystyrene-*b*-poly(methyl methacrylate) (PS-*b*-PMMA)) may be suitable for top-down processing such as etching masks or pattern transfer[41]but may not stand for a high-temperature dewetting process. Therefore, we, on purpose, choose PS-*b*-PDMS, BCP films containing Si, and carry out reactive oxygen ion etching on the BCP films so that PDMS can be transferred into well-defined SiOC with robust thermal stability. In addition, we perform thermal annealing to form spheres[42] instead of solvent treatment, preferred for micelles.[43]

3.2 Preparation of SiOC template

With the treatment time period of O_2 plasma equal to 10, 20, and 30 seconds, we prepare Template A, Template B, and Template C, respectively. In Fig. 2(a)–(c) we show the topographic images, measured by AFM, of the three prepared templates. In Template A, we can observe the ordered hemisphere array [Fig. 2(a)]. As the treatment time period increases, a similar hemisphere array is shown with the increased height contrast [Fig. 2(b) and (c)], suggesting the decrease in the PS-layer thickness. Fig. 2(d)–(f)illustrate the AFM height profiles of Template A, Template B, and Template C, respectively. These relative height profiles are obtained from the regions of the black lines shown in the corresponding topographic images [Fig. 2(a)–(c)]. All profiles exhibit rounded bulges with varied heights. The average heights of bulges in various templates are related to the O_2-plasma treatment time. The increased height in Template C is consistent with the reduced thickness of the PS matrix by increasing the O_2-plasma treatment time. This also suggests the increase in the surface ratio of SiOC hemispheres to the PS matrix. In addition, the AFM images reveal closely connected bulges for all templates [Fig. 2(d)–(f)]. Since the tip convolution effect in AFM could underestimate the sphere interspace, we further investigate the template morphology using transmission electron microscopy (TEM). In Fig. 2(g), we illustrate the TEM plan-view image of Template C. Similar to the topography shown in the AFM image [Fig. 2(c)], we can observe a single-layered sphere array (*i.e.* film thickness is around 40 nm) in hexagonal packing but with a more widened sphere interspace. The difference between the AFM image and the TEM image is attributed to the low aspect ratio of the AFM scanning probe. From the TEM image [Fig. 2(g)], the average diameter and center-to-

center distance of spheres in Template C are 25.56 ± 2.47 and 39.80 ± 3.95 nm, respectively. Consequently, the template surface can be divided into two distinct regions: one is the region with SiOC hemispheres and another one is the PS matrix. With increasing the oxygen plasma treatment time, the height of SiOC is increased, therefore, the corresponding SiOC surface area is increased.

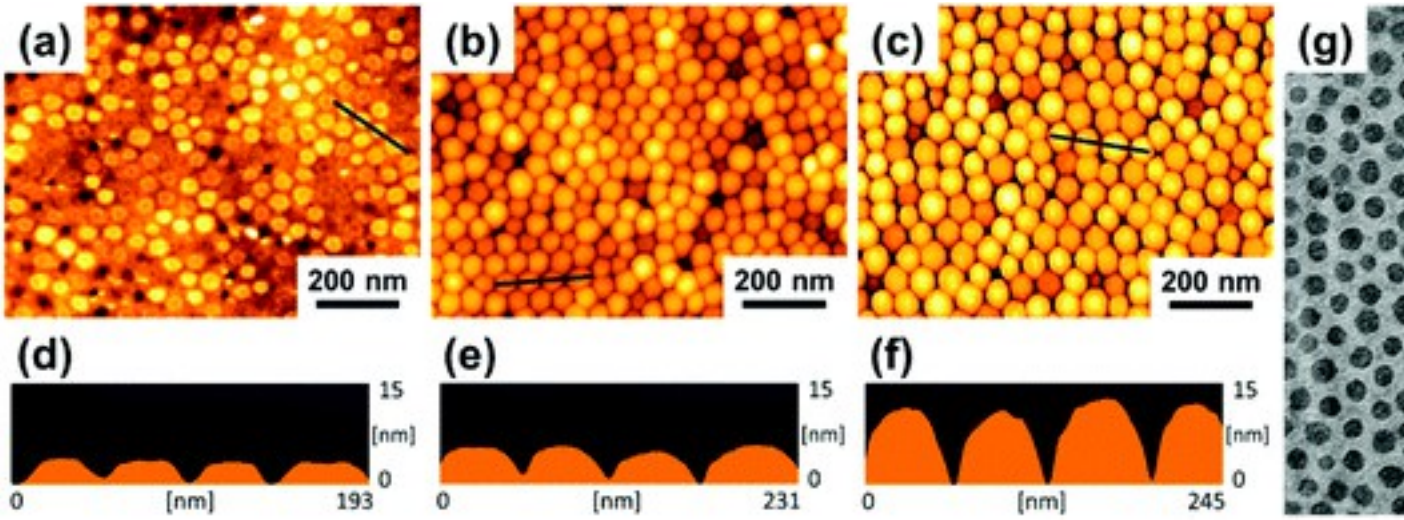

Fig. 2 AFM height images of the block copolymer templates after the O_2 plasma treatment with the time period [Template A], (b) 20 seconds [Template B], and (c) 30 seconds [Template C], respectively. The corresponding h in (d)–(f). The solid lines in the height images indicate the regions for the height profiles. The TEM plan-view i shown in (g).

3.3 Thermal dewetting of FePt on different templates

To investigate the effects of the surface ratio of the SiOC hemispheres on the PS matrix, we deposit a 2 nm-thick FePt layer on top of these three templates as well as a flat Si|SiO_2 substrate, followed by rapid-thermal annealing at 800 °C for 10 seconds with a constant heating rate of 50 °C s^{-1}. Fig. 3(a)–(d) illustrate the TEM plan-view images of the annealed FePt films grown on a flat Si|SiO_2 substrate, Template A, Template B, and Template C, respectively. The results show that on a flat substrate the dewetting of FePt films results in nanoparticles distributed randomly in space [Fig. 3(a)]. The average diameter of particles is 12.11 ± 3.4 nm (28%). A similar pattern is shown for the FePt film dewetted on Template A [Fig. 3(b)]. On Template B, we can observe a hexagonal-packed particle array with numerous stripes and islands between particles [Fig. 3(c)], while most stripes disappear in the array assembled on Template C [Fig. 3(d)], giving nanoparticles with an average diameter and center-to-center distance of 19.30 ± 2.09 nm (11%) and 39.85 ± 4.80 nm (12%), respectively. Both the hexagonal order and the center-to-center distance in the resulting particle array are nearly equal to those of the SiOC hemisphere arrays on Template C [Fig. 2(g)], suggesting that on this template the assembly of nanoparticles follows the positions of the hemisphere arrays. Further quantitative analysis is demonstrated in Fig. 3(e) and (f). During the thermal dewetting process on heterogeneous templates

(PS + SiOC hemispheres), FePt may be located in a region either on the SiOC hemispheres or in the area between hemispheres (on PS). We define the surface area ratio and the surface density based on our TEM micrographs (Fig. 3(a–d)). The surface area ratio is calculated by normalizing the area of FePt nanoparticles localized on the top of SiOC hemispheres to the total area of FePt (*i.e.* localized FePt nanoparticles and residual stripes). The surface density is calculated by normalizing the total number of nanoparticles to the total surface area. The comparison of the surface area ratio is depicted in Fig. 3(e) and the variations of surface density with the etching time are shown in Fig. 3(f). In the case of the flat substrate (Fig. 3(a)), the surface area ratio is zero due to the non-existence of the SiOC template and the surface density is about 3.16×10^{-3} nm^{-2}. For the FePt film dewetted on Template A (*i.e.*etching time = 10 s), the surface area ratio is 41.9% and the surface density is 3.23×10^{-3} nm^{-2}. The relatively small surface area ratio is attributed to the randomly dewetting of FePt on the chemically heterogeneous surface with a large residual PS matrix. With the increase of etching time to 20 s (Template B), the surface area ratio is increased to 83.4% while the surface density is 2.78×10^{-3} nm^{-2}. The increase of the surface area ratio suggests the agglomeration of the remaining stripes as well as islands occurs and the FePt atoms move to the top of the SiOC hemispheres. Most stripes disappear in the array assembled on Template C, giving a surface area ratio of 93.8% and a surface density of 1.48×10^{-3} nm^{-2}. Note that the surface density is decreased with the etching time and nearly equal to the surface density of the SiOC (1.32×10^{-3} nm^{-2}) template while the surface area ratio is increased with the etching time, suggesting the success of template-dewetting of FePt on the top of the SiOC hemispheres.

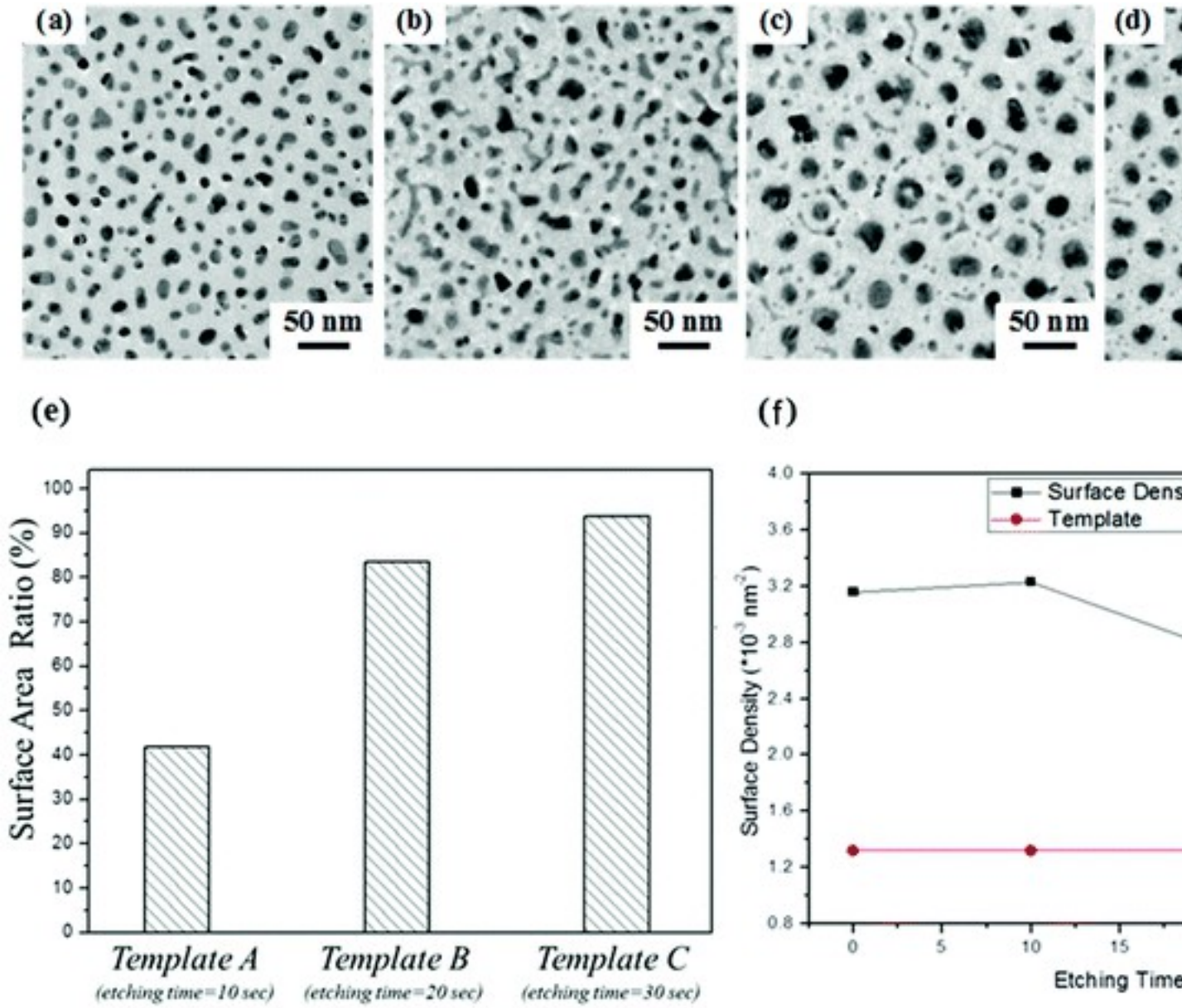

Fig. 3 TEM plan-view images of rapid-thermal annealed FePt films grown on (a) a flat Si|SiO_2 substrate, (b) Ter
and (d) Template C, respectively. (e) Surface area ratio of Template A (etching time = 10 s), Template B (etching
Template C (etching time = 30 s). (f) Surface density of FePt nanoparticles (black line) and SiOC template (red

In Fig. 4(a), we illustrate the TEM cross-sectional image of the hexagonal periodic array self-assembled on Template C. To highlight the top surfaces of this particle–template system, for the TEM cross-sectional samples, we purposely deposit an Al capping layer after post-annealing. As revealed in Fig. 4(a), the volcano-shape composite FePt/SiOC nanoparticles are aligned well by the template hemispheres, which possess a convex surface relative

to the substrate surface. Furthermore, these particles possess varied shapes of cross sections. Fig. 4(b) and (c) show the high-resolution TEM cross-sectional images of two representative particles with cross sections of different shapes. In the rounded particle, we observe (111) textures [Fig. 4(b)], while a (001) preferred orientation is observed in the particle with the elongated shape [Fig. 4(c)]. The results suggest that the dewetted particles possess either (111) or (001) textures, and the cross-sectional shape of particles could be related to the crystalline texture. This relationship needs to be further investigated to reveal the single texture among nanoparticles, which can be quite beneficial for some applications, for example, the (001)-textured magnetic patterned media.

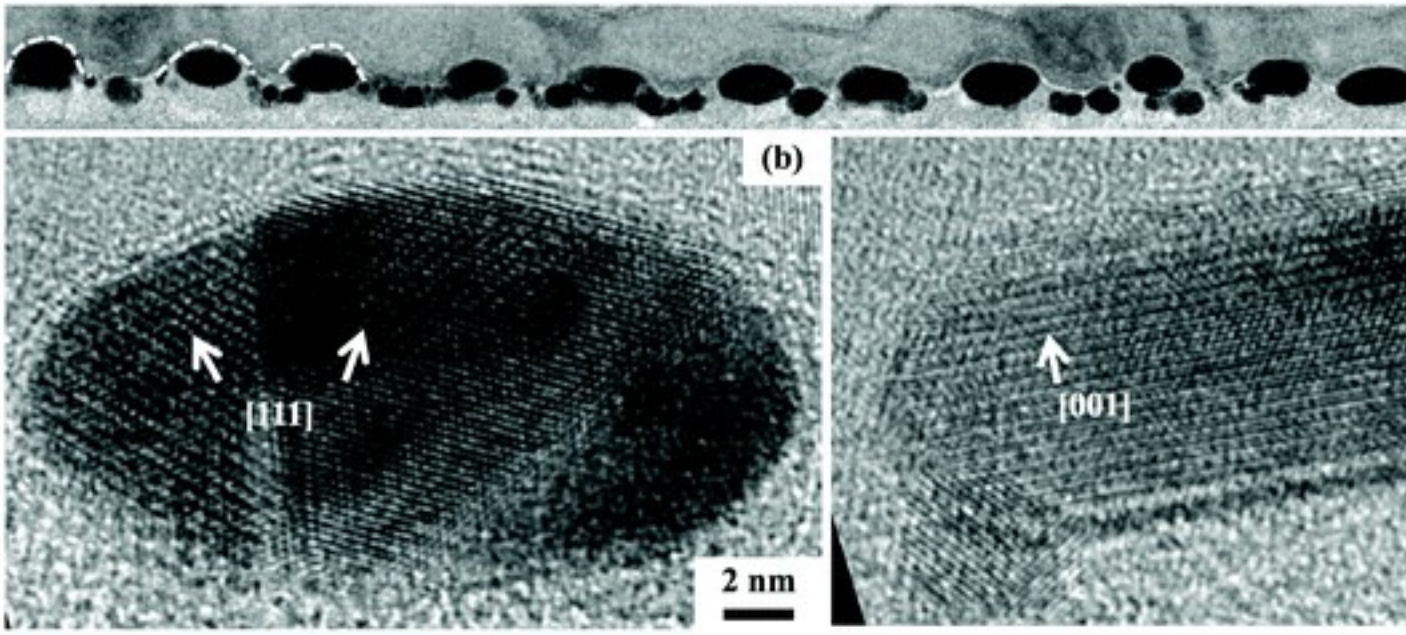

Fig. 4 (a) TEM cross-sectional image of the particle array grown on Template C. The dashed curves indicate the FePt/SiOC composite nanoparticles. The corresponding high-resolution TEM images of two representative parti (c). The arrows denote the texture orientations of the particles.

We note that the high-temperature annealing process would carbonize the PS matrix. This would give a template with a chemically heterogeneous surface, composed of SiOC hemispheres and carbon regions. Therefore, the varied nano-patterns on the abovementioned three templates may result

from the change of the interface ratio of SiOC/FePt to PS (or C)/FePt as well as the local surface curvature [Fig. 2(d)–(f)] created by the differently exposed SiOC hemispheres. We first investigate the effects of SiOC/FePt and PS/FePt interfaces on the resulting patterns by preparing samples with either interfaces but with the flat sample surface. The layer structure of the prepared samples is Si|SiO_2 substrate/PS (0 or 40 nm)/FePt (5 nm). The rapid-thermal annealing process, same as previously used, is performed for these two samples. Here we assume that the properties of the SiO_2/FePt interface are very similar to that of SiOC/FePt. Therefore, these samples with a flat surface are used to explore the effects of chemically heterogeneous interfaces and exclude the effects of the local surface curvature on thermal dewetting. We also note that only for these two samples we purposely increase the thickness of the FePt layer from 2 to 5 nm. This would give us a better signal-to-noise ratio for the subsequent structural measurements by X-ray diffraction (XRD). In ESI Fig. S1(a),† we illustrate the wide-angle XRD scans of the annealed samples with and without the PS insertion layer, respectively. The scan of the sample without the PS layer shows the (001) and (002) peak reflections, suggesting the formation of $L1_0$ ordering in the FePt layer after annealing. However, both peak reflections are not observed in the scan of the sample with the PS layer, indicating that the PS/FePt interface deteriorates the $L1_0$ ordering of FePt. Fig. S1(b) and (c)† show the TEM plan-view images of samples with and without the PS layer, respectively. While the sample with the PS layer shows the FePt stripes [Fig. S1(b)†], the FePt nanoparticles are observed for the sample without the PS layer [Fig. S1(c)†]. It has been reported that in the case of FePt films, the interface diffusion rate promotes both the degree of $L1_0$ ordering and the film agglomeration.[44] Here the increased film continuity along with the deteriorated degree of $L1_0$ ordering of the FePt film grown on the PS layer

suggest that the surface diffusion rate of FePt atoms on the PS surface could be slower than that on the SiO_2 surface. As a result, the PS layer suppresses the dewetting of the FePt film after annealing. For Templates B and C, the increased oxygen plasma time increases the SiOC/FePt to PS (or C)/FePt ratio. Therefore, compared with the dewetted FePt patterns with the remaining stripes between hemispheres on Template B [Fig. 3(c)], the decreased PS/FePt interface area on Template C would suppress the formation of these stripes [Fig. 3(d)].

The cross-sectional TEM image [Fig. 4(a)] clearly reveals that the FePt nanoparticles formed on Template C are located on the top of the SiOC hemispheres, which possess a convex surface relative to the PS surface. As the surface chemical potential is known to be proportional to the curvature of the substrate surface,[26] the convex surface at the top of the SiOC hemisphere should possess a positive excess chemical potential compared to the flat PS regions, giving energetically unfavorable sites for FePt nanoparticles. Because our nano-template is composed of a PS matrix and SiOC hemispheres, in addition to the curvature-induced chemical potential difference, we need to consider other energies associated with this chemically heterogeneous template. We have shown that, in ESI Fig. S1(b) and (c),† the different dewetted patterns suggest that the surface diffusion rate of FePt atoms on PS (or C) is lower than that on SiOC. This implies that the bonding between FePt and PS (or C) might be stronger. Consequently, the bonding energy difference may also prefer the FePt nanoparticles to be formed on the PS matrix and cannot be used to explain the observed results.

Recall that the varied amounts of strain energy exerted on films can further manipulate the surface chemical potential; dewetted nanoparticles prefer to form in regions with less strain energy.[29] Here we have utilized the annealing process combining a rapid thermal annealing process with a Si

substrate as an infrared light absorber.[45] This annealing process has been previously demonstrated to provide a thermal expansion of the Si substrate different from that of the FePt film, therefore leading to strain energy exertion on the FePt films during annealing.[45] In addition, the amount of strain energy increases with increasing the heating rate of the RTA process because of the increased transient light intensity from the infrared heating lamp.[45] Therefore, this would provide a tuning knob to adjust the strain energy of films and enable us to study the behaviors of the template dewetting under different strain energies by varying the heating rates. To do this, we anneal a 2 nm-thick FePt film grown on Template C by RTA with a reduced heating rate of 20 °C s^{-1}. In ESI Fig. S2,† we show the corresponding TEM plan-view image. Different from the previous array annealed with a heating rate of 50 °C s^{-1} [Fig. 3(d)], the reduced heating rate significantly increases the amounts of stripes between particles. Since the curvature and the PS/SiOC area ratio are kept the same for the identical template, the observed morphology modification is mainly attributed to the changes of strain energy by different heating rates. We have shown a high degree of ordering with a strong (001) texture of FePt nanoparticles on the SiO_2 surface [ESI Fig. S1(a) and (c)†]. On the other hand, FePt with a low degree of ordering is obtained when grown on the PS (or C) layer [ESI Fig. S1(a) and (b)†] due to a low surface diffusion rate. According to previous simulations,[46] when a FePt film is under in-plane tensile stress, the phase transformation from a disordered state to a highly ordered (001) texture leads to the largest strain relaxation, and hence the lowest strain energy state. The RTA process with a Si substrate provides in-plane tensile stress[45-47] and this stored strain energy can be relaxed by the ordering process of FePt. Consequently, when the FePt nanoparticles are located on the top of SiOC hemispheres, the high ordering process significantly reduced the local

strain energy and may overcome the curvature-induced chemical potential to reach a local energy minimum. When the heating rate is reduced, the induced in-plane tensile stress is decreased accordingly, leading to the reduced degree of ordering of FePt films.[45] Recall that the total surface chemical potential of films is the sum of the surface chemical potential on the flat template surface, surface curvature-contributed chemical potential and local strain energy.[29] Therefore, with the reduced stored strain energy and less strain energy relaxation by decreasing the heating rate, the strain energy term could become less significant and the first two terms increase the amounts of FePt stripes on the PS matrix [ESI Fig. 2†].

3.4 *In situ* TEM observation

To further understand the morphology evolution of films during dewetting, we monitor the film morphology in real-time at varied temperatures using TEM with an *in situ* heating stage. For this TEM observation we prepare Template C on the Si_3N_4|SiO_2membrane, followed by the deposition of a 2 nm-thick FePt layer at ambient temperature. This membrane allows us to directly investigate the film morphologies by TEM without any further preparation process, *e.g.*, sample grinding or ion milling, which could induce defects in the as-deposited films and therefore change the subsequent dewetting behavior at elevated temperatures. During the TEM observation, we raise the sample temperature with a heating rate of 50 °C min^{-1}. Compared with the heating rate of 50 °C s^{-1} for the RTA process, this heating rate, limited by the heating holder, is much lower. Therefore in the following we will only present the evolution of dewetted patterns under a relatively low strain energy, *i.e.*, a hexagonal periodic array with stripes between spheres [Fig. S2†]. In Fig. 5(a)–(d), we illustrate the resulting TEM plan-view images at temperatures of ambient temperature, 600 °C, 700 °C, and 800 °C, respectively. For all images we intentionally choose the sample area with a black spot at the bottom left as the marker, which enables us to observe the film morphology on an identical sample area. Similar to the template prepared on the Si substrate [Fig. 2(g)], we observe a hexagonal periodic array of SiOC spheres in the as-deposited state [Fig. 5(a)]. We note that at this stage the morphology of the as-deposited FePt film could be continuous, therefore contributing little contrast to the TEM image. Upon heating to 600 °C, the sphere sizes are slightly reduced while some stripes are shown around spheres [Fig. 5(b) and the inset of Fig. 5(b)], suggesting that the dewetting process is initiated by rupturing films at the edges of SiOC hemispheres. Raising the temperature to 800 °C continuously shrinks the particle sizes and increases the number of stripes surrounding the spheres [Fig. 5(c) and

(d) and the insets of Fig. 5(c) and (d)]. This indicates that at elevated temperatures the thermal energy drives films to aggregate to both the top of the SiOC hemispheres and the area between hemispheres. These two positions of the template could possess similar chemical potentials during the annealing process with a low heating rate. When we increase the heating rate to 50 °C s^{-1}, we believe that the morphology evolution should be similar to that observed in Fig. 5, except for the reduced number of strips.

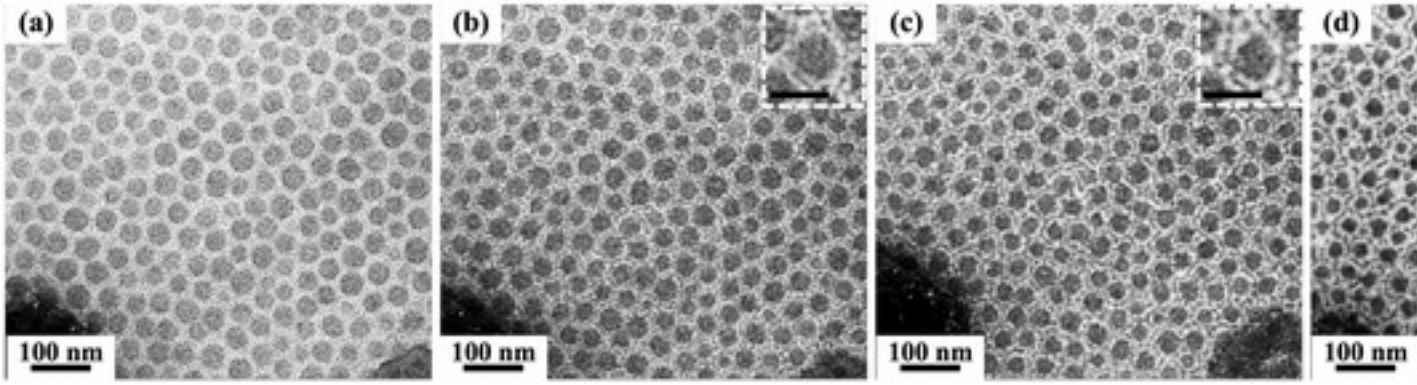

Fig. 5 TEM plan-view images of the FePt film *in situ* annealed by using a TEM heating stage at temperatures of (b) 600 °C, (c) 700 °C, and (d) 800 °C. Insets in (b)–(d) are the TEM plan-view images of the representative par corresponding temperatures (scale bar = 50 nm).

In the reported studies,[48–50] when the thermal dewetting takes place on a relatively flat and homogeneous surface, the particles agglomerate and the particle size is increased with increasing annealing temperature. Unlike the situations reported previously, our substrate possesses a heterogeneous surface with lateral morphological variations, therefore, the temperature dependence of the particle size does not follow the same trend as reported.[48–50] Our *in situ* TEM images clearly reveal that the film ruptures at the edges of SiOC hemispheres at 600 °C and at elevated temperatures the thermal energy drives films to aggregate to both the top of the SiOC hemispheres and the area between hemispheres. When we only count the projection size of FePt nanoparticles on top of the SiOC hemispheres in Fig. 5(b)–(d), we find that the size decreases with increasing annealing temperature (23.6 nm, 21.3 nm and 18.2 nm for samples annealed at 600, 700 and 800 °C, respectively), different from the reported results.[48–50] The different trend can be explained by the confinement of SiOC hemispheres and strain energy-induced dewetting, which prevent particle coarsening.

The *in situ* TEM observation confirms that the positions of nanoparticles are aligned with those of the SiOC hemispheres; therefore, further increasing the SiOC density may increase the nanoparticle density accordingly. Furthermore, for the TEM samples, the nano-templates are fabricated on the $Si_3N_4|SiO_2$ membrane instead of Si substrates. This in fact demonstrates the unique ingredients of our proposed approach different from the reported ones: we can fabricate our nano-templates to widely available substrates which can absorb infrared light during RTA. For example, a polycrystalline Si layer deposited on glass substrates has been reported to induce similar stress on FePt[45] so our nano-templates can also be fabricated on glass substrates.

3.5 Magnetic properties

Finally we investigate the magnetic properties of the FePt hexagonal periodic array because FePt, specifically in the ordered $L1_0$phase, possesses broad applications in magnetic devices, *e.g.*, magnetic recording media. Fig. 6 shows both the out-of-plane and in-plane hysteresis loops of the hexagonal periodic array grown on Template C. Both the out-of-plane and the in-plane coercivity values are nearly equal to around 15 kOe. This large coercivity value indicates the phase transformation of FePt from a disordered A1 to an ordered $L1_0$ phase after RTA. In fact, the same BCP films (PS-*b*-PDMS) have been utilized as the etching mask for FePt films for obtaining nano-dots but much lower coercivity (~6 kOe) was obtained due to etching damage.[51]Furthermore, the equally out-of-plane and in-plane coercivity values suggest the co-existence of (111) and (001) textures in the particles. This is consistent with the TEM observation of various textures in the different-shaped nanoparticles [Fig. 4(b) and (c)]. The hexagonal array of FePt nanoparticles reveals a large coercivity of 1.5 T, much larger than the nanoparticles fabricated by top-down approaches.[51–55] Most of the top-down methods use either e-beam lithography,[53,55] nanoimprinting[52] or the self-assembled co-polymer[51,54] to define the pattern size of masks. All of them need to use ion etching for pattern transferring, and the ion damage usually causes the reduction of coercivity due to the disordering of the FePt $L1_0$ structure as the high coercivity of FePt is believed to originate from the $L1_0$ atomic ordering structure.[56] The ion damage in the nanodots consisting of the $[Co/Pd]_n$ multilayer has been identified from the contrast difference between the center and the edge regions of dots revealed in TEM plan-view images, and the reduced coercivity is observed in the dots with damaged edges.[14] When an ordered FePt continuous film is patterned into nanostructures by the conventional etching process, the high energy ion

bombardment during the etching process can also cause severe atomic disorder of the $L1_0$ lattice in damaged edges and therefore reduce the coercivity accordingly. Because our approach does not require the etching process to form nanostructures, we can completely eliminate the ion etching damage and achieve a high coercivity. We also note that in the application of magnetic recording media, the read-back signals from written bits really depend on the spatial order of magnetic bits. Therefore, the FePt nanoparticles with spatial disorder are very difficult for addressing and reading, and the much improved spatial order of FePt nanoparticles presented here may be potentially used for magnetic media. By further investigating the shape control of nanoparticles during the dewetting, we may have a chance to further tune the texture of individual particles and therefore to manipulate the magnetic properties.

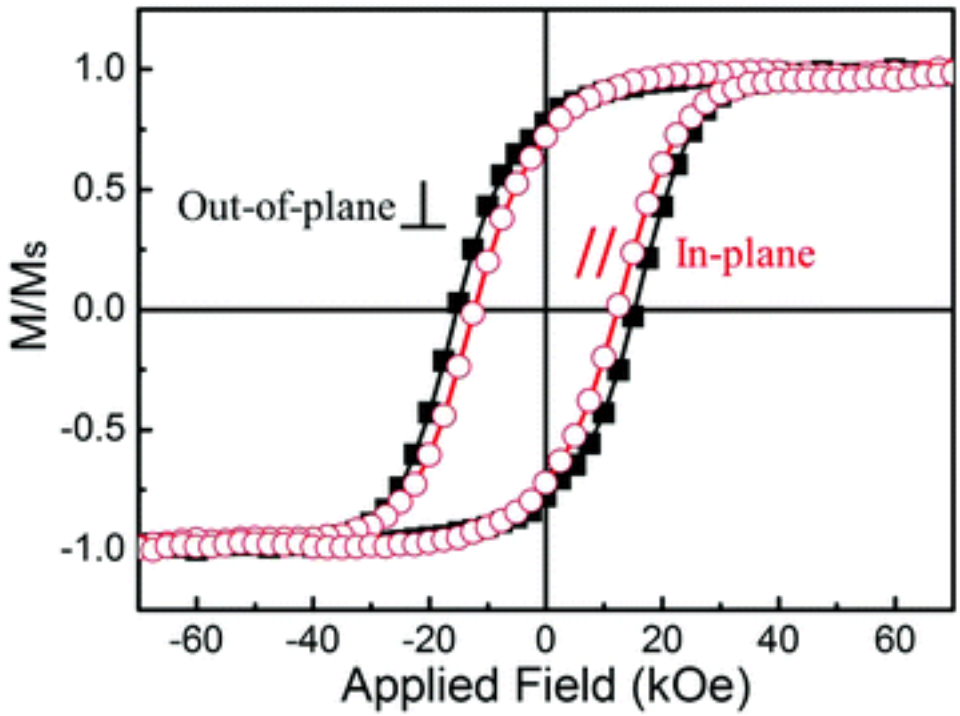

Fig. 6 Out-of-plane and in-plane hysteresis loops of the FePt hexagonal periodic arrays grown on Template C.

4. Conclusions

To summarize, we propose a chemically heterogeneous nano-template for thermal dewetting to obtain self-assembled $L1_0$nanoparticle arrays. Several novelties are demonstrated by our proposed templated thermal dewetting, and are summarized as follows:

(1) a chemically heterogeneous template, composed of a hexagonal periodic array of SiOC hemispheres emerging from a polystyrene matrix, enables us to vary the interfacial diffusion rate and the strain energy of FePt in different regions (SiOC/FePt and PS/FePt), which cannot be achieved simply

by the commonly reported heterogeneous templates. (2) Large-area self-assembled SiOC hemispheres enable us to reach the size of FePt nanoparticles below 20 nm, which cannot be easily obtained in the template made by photolithography. (3) The lateral strain energy difference, caused by the FePt structural transformation instead of a lattice mismatch between the films and substrates, is used to drive the formation of FePt nanoparticles located on the top of SiOC hemispheres rather than in the valley or flat regions of templates.

Because of the spatially modulated chemical compositions on the template surface, the driving force for the thermal dewetting can be adjusted by various contributions, including surface chemical potential on the flat template surface, surface curvature-induced chemical potential and local strain energy. By reducing the PS (or C)/FePt interface area, which possesses a lower surface diffusion rate than the SiOC/FePt interface, we can decrease the remaining FePt stripes on the PS matrix. These stripes can be further reduced by increasing the heating rate of the RTA process, which increases the strain energy difference between different regions, leading to hexagonal periodic arrays of $L1_0$ FePt nanoparticles assembled by SiOC hemispheres. The *in situ* TEM observation reveals the evolution of the dewetting process, and confirms that the positions of nanoparticles are aligned with those of the SiOC hemispheres. The self-assembled FePt nanoparticles reveal a large coercivity, indicating that the film agglomeration and structure ordering occur simultaneously. As the density and regularity of SiOC hemispheres can be further improved by optimizing the process for both the block copolymer and RIE etching, the presented approach provides an efficient pathway for the fabrication of metallic nanoparticles in a wide range of material systems. Furthermore, compared with the nano-template with a single interfacial composition, for example, Si or AAO, the proposed chemically heterogeneous

template offers more degrees of freedom to locate the nanoparticles for various applications. We believe that we successfully pave an avenue for obtaining a regular array of metallic nanoparticles with simplicity, versatility and low-cost.

Acknowledgements

The financial support of the Ministry of Science and Technology under Grant No. NSC 102-2221-E-007-044-MY2 and MOST 103-2633-M-007-001 is gratefully acknowledged. The support of the Hsinchu Science Park of Republic of China under Grant No. 103A06 is also acknowledged.

References

1. C. A. Rose, *Annu. Rev. Mater. Res.*, 2001, **31**, 203–235 CrossRef .
2. C. J. Cheng, C. A. Rose, V. Z.-H. Chan, E. L. Thomas, R. G. H. Lammerink and G. J. Vancso, *Adv. Mater.*, 2001, **13**, 1174–1178 CrossRef .
3. K. Naito, H. Hieda, M. Sakurai, Y. Kamata and K. Asakawa, *IEEE Trans. Magn.*, 2002, **38**, 1949–1951 CrossRef CAS .

4. S. A. Maier, M. L. Brongersma, P. G. Kik, S. Meltzer, A. A. G. Requicha and H. A. Atwater, *Adv. Mater.*, 2001, **13**, 1501–1505 CrossRef CAS.
5. S. A. Maier and H. A. Atwater, *J. Appl. Phys.*, 2005, **98**, 011101 CrossRef.
6. A. F. Koenderink, *Nano Lett.*, 2009, **9**, 4228–4233 CrossRef CAS PubMed.
7. R. S. Wagner and W. C. Ellis, *Appl. Phys. Lett.*, 1964, **4**, 89–90 CrossRef CAS.

8. K. A. Dick, K. Deppert, L. S. Karlsson, W. Seifert, L. R. Wallenberg and L. Samuelson, *Nano Lett.*, 2006, **6**, 2842–2847 CrossRef CAS PubMed .
9. Y. F. Guan, R. C. Pearce, A. V. Melechko, D. K. Hensley, M. L. Simpson and P. D. Rack, *Nanotechnology*, 2008, **19**, 235604 CrossRef CAS PubMed .
10. Y. Nakayama, S. Okazaki, N. Saitou and H. Wakabayashi, *J. Vac. Sci. Technol., B*, 1990, **8**, 1836–1840 CAS .
11. S. S. Shankar, L. Rizzello, R. Cingolani, R. Rinaldi and P. P. Pompa, *ACS Nano*, 2009, **3**, 893–900 CrossRef CAS PubMed .

12. T. Ito and S. Okazaki, *Nature*, 2000, **406**, 1027–1031 CrossRef CAS PubMed .
13. S. Sun, C. B. Murray, D. Weller, L. Folks and M. Moser, *Science*, 2000, **287**, 1989–1992 CrossRef CAS PubMed .
14. J. W. Lau, X. Liu, R. C. Boling and J. M. Shaw, *Phys. Rev. B: Condens. Matter*, 2011, **84**, 214427 CrossRef .
15. J.-W. Liao, U. Atxitia, R. F. L. Evans, R. W. Chantrell and C.-H. Lai, *Phys. Rev. B: Condens. Matter*, 2014, **90**, 174415 CrossRef .

16. M. S. She, T. Y. Lo, H. Y. Hsueh and R. M. Ho, *NPG Asia Mater.*, 2013, **5**, e42 CrossRef CAS .
17. H. Krishna, R. Sachan, J. Strader, C. Favazza, M. Khenner and R. Kalyanaraman, *Nanotechnology*, 2010, **21**, 155601 CrossRef CAS PubMed .
18. S.-H. Kwon, D.-H. Han, H. J. Choe and J.-J. Lee, *Nanotechnology*, 2011, **22**, 245608 CrossRef PubMed .
19. C. V. Thompson, *Annu. Rev. Mater. Res.*, 2012, **42**, 399–434 CrossRef CAS .

20. Y.-C. Wu, L.-W. Wang, M. T. Rahman and C.-H. Lai, *J. Appl. Phys.*, 2008, **103**, 07E126 Search PubMed.
21. A. L. Giermann and C. V. Thompson, *Appl. Phys. Lett.*, 2005, **86**, 121903 CrossRef.
22. Y. J. Oh, C. A. Ross, Y. S. Jung, Y. Wang and C. V. Thompson, *Small*, 2009, **5**, 860–865 CrossRef CAS PubMed.
23. Y. J. Oh, J. H. Kim, C. V. Thompson and C. A. Ross, *Nanoscale*, 2013, **5**, 401–407 RSC.

24. S. Yang, F. Xu, S. Ostendorp, G. Wilde, H. Zhao and Y. Lei, *Adv. Funct. Mater.*, 2011, **21**, 2446–2455 CrossRef CAS.
25. E. R. Meshot, Z. Zhao, W. Lu and A. J. Hart, *Nanoscale*, 2014, **6**, 10106–10112 RSC.
26. W. W. Mullins, *J. Appl. Phys.*, 1957, **28**, 333–339 CrossRef CAS.
27. D. C. Abeysinghe, W. Chen, Q. Zhan and R. E. Nelson, *Nanotechnology*, 2009, **20**, 475301 CrossRef PubMed.

28. F. Ruffino, V. Torrisi, G. Marletta and M. G. Grimaldi, *J. Appl. Phys.*, 2012, **112**, 124316 CrossRef.
29. B. Yang, F. Liu and M. G. Lagally, *Phys. Rev. Lett.*, 2004, **92**, 025502 CrossRef PubMed.
30. S. Sun, *Adv. Mater.*, 2006, **18**, 393–403 CrossRef CAS.
31. F. Schäffel, C. Täschner, M. H. Rümmeli, V. Neu, U. Wolff, U. Queitsch, D. Pohl, R. Kaltofen, A. Leonhardt, B. Rellinghaus, B. Büchner and L. Schultz, *Appl. Phys. Lett.*, 2009, **94**, 193107 CrossRef.

32. J. Wu, A. Gross and H. Yang, *Nano Lett.*, 2011, **11**, 798–802 CrossRef CAS PubMed.
33. S. Guo and S. Sun, *J. Am. Chem. Soc.*, 2012, **134**, 2492–2495 CrossRef CAS PubMed.
34. S. Kuo, D. Li, H. Zhu, S. Zhang, N. M. Markovic, V. R. Stamenkovic and S. Sun, *Angew. Chem., Int. Ed.*, 2013, **52**, 3465–3468 CrossRef PubMed.
35. V. Mazumder, M. Chi, K. L. More and S. Sun, *J. Am. Chem. Soc.*, 2010, **132**, 7848–7849 CrossRef CAS PubMed.

36. Y.-C. Wu, L.-W. Wang and L.-W. C.-H. Lai, *Appl. Phys. Lett.*, 2008, **93**, 242501 CrossRef .
37. J.-P. Wang, *Proc. IEEE*, 2008, **96**, 1847–1863 CrossRef CAS .
38. M. Brinkmann, V. Z.-H. Chan and E. L. Thomas, *Chem. Mater.*, 2001, **13**, 967–972 CrossRef CAS .
39. C. C. Chao, R. M. Ho, P. Georgopanos, A. Avgeropoulos and E. L. Thomas, *Soft Matter*, 2010, **6**, 3582–3587 RSC .

40. C. C. Chao, T. C. Wang, R. M. Ho, P. Georgopanos, A. Avgeropoulos and E. L. Thomas, *ACS Nano*, 2010, **4**, 2088–2094 CrossRef CAS PubMed.
41. R. A. Farrell, N. Kehagias, M. T. Shaw, V. Reboud and M. Zelsmann, *ACS Nano*, 2011, **5**, 1073–1085 CrossRef CAS PubMed.
42. W. I. Park, J. M. Yoon, M. Park, J. Lee, S. K. Kim, J. W. Jeong, K. Kim, H. Y. Jeong, S. Jeon, K. S. No, J. Y. Lee and Y. S. Jung,*Nano Lett.*, 2012, **12**, 1235–1240 CrossRef CAS PubMed.
43. Z. Chen, C. He, F. Li, L. Tong, X. Liao and Y. Wang, *Langmuir*, 2010, **26**, 8869–8874 CrossRef CAS PubMed.

44. J.-W. Liao, K.-F. Huang, L.-W. Wang, W.-C. Tsai, W.-C. Wen, C.-C. Chiang, H.-J. Lin, F.-H. Chang and C.-H. Lai, *Appl. Phys. Lett.*, 2013, **102**, 062420 CrossRef .
45. L.-W. Wang, W.-C. Shin, Y.-C. Wu and C.-H. Lai, *Appl. Phys. Lett.*, 2012, **101**, 252403 CrossRef .
46. J. S. Kim, Y. M. Kuo and B. J. Lee, *J. Appl. Phys.*, 2006, **99**, 053906 CrossRef .
47. M. Albrecht and C. Brombacher, *Phys. Status Solidi A*, 2013, **210**, 1272–1281 CrossRef CAS .

48. F. Ruffino and M. G. Grimaldi, *Physica E*, 2015, **69**, 121–126 CrossRef CAS.
49. F. Ruffino and M. G. Grimaldi, *Appl. Surf. Sci.*, 2013, **270**, 697–706 CrossRef CAS.
50. M. Aouassa, L. Favre, A. Ronda, H. Maaref and I. Berbezier, *New J. Phys.*, 2012, **14**, 063038 CrossRef.
51. A. Kikitsu, T. Maeda, H. Hieda, R. Yamamoto, N. Kihara and Y. Kamata, *IEEE Trans. Magn.*, 2013, **49**, 693 CrossRef CAS.

52. Z. Li, W. Zhang and K. M. Krishnan, *AIP Adv.*, 2015, **5**, 087165 CrossRef.
53. T. Shimatsu, Y. Inaba, H. Kataoka, J. Sayama, H. Aoi, S. Okamoto and O. Kitakami, *J. Appl. Phys.*, 2011, **109**, 07B726 CrossRef.
54. H. Wang, M. T. Rahman, H. Zhao, Y. Isowaki, Y. Kamata, A. Kikitsu and J. P. Wang, *J. Appl. Phys.*, 2011, **109**, 07B754 Search PubMed.
55. A. T. McCallum, P. Krone, F. Springer, C. Brombacher, M. Albrecht, E. Dobisz, M. Grobis, D. Weller and O. Hellwig, *Appl. Phys. Lett.*, 2011, **98**, 242503 CrossRef.

56. C. B. Rong, D. Li, V. Nandwana, N. Poudyal, Y. Ding, Z. L. Wang, H. Zeng and J. P. Liu, *Adv. Mater.*, 2006, **18**, 2984–2988 CrossRef CAS .